Comparison between Spectral-domain and Swept-source OCT Angiography Scans for the Measurement of Hyperreflective Foci in Age-related Macular Degeneration

Gissel Herrera, MD,[1] Yuxuan Cheng, PhD,[2] Yamini Attiku, MD,[1] Farhan E. Hiya, MD,[1] Mengxi Shen, MD, PhD,[1] Jeremy Liu, MD,[1,3] Jie Lu, PhD,[2] Alessandro Berni, MD,[1,4] Omer Trivizki, MD,[1,5] Jianqing Li, MD,[1,6] Robert C. O'Brien, PhD,[1] Giovanni Gregori, PhD,[1] Ruikang K. Wang, PhD,[2,7] Philip J. Rosenfeld, MD, PhD[1]

Purpose: Spectral-domain OCT angiography (SD-OCTA) scans were used in an algorithm developed for swept-source OCT angiography (SS-OCTA) scans to determine if SD-OCTA scans yielded similar results for the measurement of hyperreflective foci (HRF) in intermediate age-related macular degeneration (iAMD).

Design: Retrospective study.

Participants: Forty eyes from 35 patients with iAMD.

Methods: Patients underwent SD-OCTA and SS-OCTA imaging at the same visit using a 6 × 6 mm OCTA scan pattern. Hyperreflective foci were detected as hypotransmission defects on en face structural images generated from a custom slab positioned 64 to 400 μm beneath Bruch's membrane and confirmed on corresponding B-scans by the presence of well circumscribed lesions within the neurosensory retina or along the retinal pigment epithelium (RPE) that are of equal or greater reflectivity than that of the RPE. Two independent graders evaluated the en face images and B-scans for the presence of these lesions. Outlines of HRF on en face images were generated using a published semiautomated algorithm developed for SS-OCTA scans and manually corrected by the graders when necessary. The total area measurements of the HRF within the 5-mm circle centered on the fovea were obtained from the algorithm using each imaging method.

Main Outcome Measures: Agreement of the square root (sqrt) of the HRF total areas obtained from SS-OCTA and SD-OCTA.

Results: The sqrt total areas of the HRF from both imaging modalities were highly concordant, with Lin's concordance correlation coefficient (r_c) of 0.94 (95% confidence interval: 0.86–0.97; $P < 0.001$). The mean sqrt of the total HRF area measurements identified using SS-OCTA and SD-OCTA imaging were 0.390 mm (standard deviation [SD]: 0.170) and 0.393 mm (SD: 0.187), respectively with mean difference of −0.003 (95% confidence interval: −0.021 to 0.015; $P=0.76$).

Conclusions: Spectral-domain OCT angiography scans yielded results similar to SS-OCTA scans when the same semiautomated algorithm was used to measure HRF in the central 5 mm of the macula, suggesting that either a single 6 × 6 mm SD-OCTA or a SS-OCTA scan pattern can be used to determine the total macular HRF burden in eyes with age-related macular degeneration.

Financial Disclosure(s): Proprietary or commercial disclosure may be found in the Footnotes and Disclosures at the end of this article. *Ophthalmology Science 2025;5:100633 © 2024 Published by Elsevier Inc. on behalf of the American Academy of Ophthalmology. This is an open access article under the CC BY-NC-ND license (http://creativecommons.org/licenses/by-nc-nd/4.0/).*

In age-related macular degeneration (AMD), macular pigmentary abnormalities were first described on fundus examination and color fundus imaging as dark foci within the macula.[1–4] When diagnosed in conjunction with medium-sized drusen, the presence of hyperpigmentation (hyperPig) was sufficient to increase the stage of AMD from early to intermediate AMD (iAMD) according to the clinical classification system proposed by Ferris et al.[5]

On OCT B-scans, macular hyperPig has been associated with the presence of hyperreflective foci (HRF), both intraretinal HRF (iHRF) and along the retinal pigment

epithelium (rpeHRF).[6,7] Typically, HRF in AMD were located at the inner border (apex) of drusen on OCT B-scans, giving the appearance of a thickened retinal pigment epithelium (RPE), which are considered to be RPE cells that have proliferated, migrated, or aggregated from their location along the monolayer into these hyperreflective regions.[6–11] Compared with rpeHRF, the iHRF are considered to be RPE aggregations that have migrated into the neurosensory retina and are characterized as well circumscribed, punctate lesions in a single or clustered distribution that are of equal or greater reflectivity than

the RPE, most often overlying drusen, but they may also appear without a clear relationship to drusen.[6,10,12−15]

Macular HRF identified on OCT images of eyes with AMD are an anatomic feature associated with an increased risk for disease progression.[8,10,12,13,16−28] The presence of these HRF are associated with the risk of forming macular atrophy[12,13,18,21,24] and the risk of developing exudation secondary to macular neovascularization.[16,17,26] Moreover, these HRF on OCT images correspond to the areas of hyperPig seen on color fundus imaging[6,7,29,30] and have been recognized as a negative prognostic biomarker for visual function.[31,32]

Using their hyperreflective properties on OCT en face images corresponding to different slabs from the inner to the outer retina, Verma et al[28] and Sadda et al[33] quantified iHRF, establishing a relationship between the spatial distribution of these lesions and the progression of iAMD.[28,33] However, this strategy fails to account for the HRF located along the RPE monolayer referred to as rpeHRF. By using en face OCT imaging from dense raster volume scans in conjunction with B-scans to detect macular hyperPig as seen in color fundus imaging, Laiginhas et al[7] were able to detect both the iHRF and rpeHRF. The en face images used in their study were generated from a slab with segmentation boundaries positioned 64 μm to 400 μm below Bruch's membrane, referred to as sub-RPE slabs. On these en face sub-RPE slabs, both iHRF and rpeHRF appear as dark lesions or hypotransmission defects (hypoTDs) caused by the complete attenuation of light penetration into the choroid as a result of the hyperreflective nature of these lesions.

While the en face imaging strategy was originally developed for use with structural spectral-domain OCT (SD-OCT) dense raster volume scans, this imaging strategy has evolved to be used with both SD-OCT angiography (SD-OCTA) and swept-source OCT angiography (SS-OCTA) scans.[7,34] The OCTA scans are ideal for en face imaging since they are generated using dense isotropically spaced B-scans with ≥2 B-scans repeated at each position and contain both structural and angiographic images.[35] OCT angiography scans have been used to study a range of structural OCT biomarkers in AMD such as macular HRF,[7,36] drusen area and volume,[37,38] calcifying drusen,[39,40] basal laminar deposits,[41] and outer retinal thickness.[42]

Given that SD-OCTA instruments are more widely available than SS-OCTA instruments, we investigated whether our semiautomatic algorithm,[36] which was developed for the detection and quantification of HRF using SS-OCTA scans, could be used on SD-OCTA scans.

Methods

Patients with AMD were enrolled in ongoing prospective, observational, swept-source OCT and SD-OCT imaging studies at the Bascom Palmer Eye Institute. The Institutional Review Board of the University of Miami Miller School of Medicine approved the study, and all patients signed an informed consent for both prospective SD-OCT and swept-source OCT studies. The study was performed in accordance with the tenets of the Declaration of Helsinki and complied with the Health Insurance Portability and Accountability Act of 1996.

A retrospective review of the prospectively enrolled subjects was performed to identify eyes with nonexudative iAMD and HRF that were imaged at the same visit on both the SS-OCTA (PLEX Elite 9000, Carl Zeiss, Meditec Inc) and SD-OCTA (Cirrus HD-OCT, Carl Zeiss, Meditec Inc) instruments using the 6 × 6 mm angiographic scan patterns centered on the fovea.

Imaging Protocols

All SD-OCTA and SS-OCTA scans were acquired by one of 2 trained imaging technicians in a random acquisition sequence. The SD-OCT instrument was powered by a superluminescent diode light source with a central wavelength of 840 nm with a scan rate of 67 000 A-scans/second. The 6 × 6 mm SD-OCTA scan pattern consisted of 350 A-scans per B-scan and 350 B-scans with each B-scan repeated twice at each position, resulting in a uniform 17 μm spacing between A-scans. The SS-OCTA instrument was powered by a swept laser source with a central wavelength of 1050 nm with a scan rate of 100 000 A-scans/second. The 6 × 6 mm SS-OCTA scan pattern consisted of 500 A-scans per B-scan and 500 B-scans with each B-scan repeated twice at each position, resulting in a uniform 12 μm spacing between A-scans. Both instruments had an optical axial resolution of ∼5 μm in tissue and an estimated transverse resolution of ∼15 μm at the retinal surface. Each volumetric scan was reviewed for quality and signal strength, and scans with a signal strength <7 based on the instrument's output as well as scans with significant motion artifacts were excluded.

In addition, eyes with evidence of atrophy in the form of persistent choroidal hypertransmission defects were excluded. Persistent hypertransmission defects were defined as areas of increased focal brightness on en face sub-RPE slab corresponding to the hypertransmission of light into the choroid with a greatest linear dimension measuring ≥250 μm.[43−45] Eyes were also excluded if they had evidence of exudation, which was defined as the appearance of any sub-RPE, subretinal, or intraretinal fluid on structural OCT B-scans and on the retinal thickness maps, or if other retinal pathologies were present, such as diabetic retinopathy, retinal vein occlusion, and central serous chorioretinopathy.

Grading of HRF

Hyperreflective foci, either iHRF or rpeHRF, were identified as hypoTDs on en face structural images generated from a custom slab positioned 64 μm to 400 μm beneath Bruch's membrane on each instrument, also known as a sub-RPE slab.[7] These hypoTDs are described on the sub-RPE en face images as areas of focally decreased signal intensity that correspond to the hypotransmission of light into the choroid (hypoTDs). All corresponding B-scans were inspected to ensure that these hypoTDs matched the position of iHRF or the rpeHRF as previously reported.[7] Other pathological features such as calcified drusen, hemorrhages, vitelliform lesions, and large retinal pigment epithelial detachments that could also lead to focal choroidal hypoTDs in eyes with iAMD[39,46] were easily excluded from the manual annotations by reviewing the corresponding B-scan through a particular hypoTD.

Two independent, masked graders (G.H. and Y.A.) initially evaluated SS-OCTA en face images and B-scans for the presence of HRF. These SS-OCTA scans together with matching same-day SD-OCTA scans were processed through a published semiautomated algorithm based on the optical attenuation coefficients and previously validated for SS-OCTA scans.[36] In a masked fashion, outlines of HRF were generated separately for both the SS-OCTA and SD-OCTA scans. These outlines were then

Table 1. Comparison between the Square Root Total Area of Hyperreflective Foci within the 5-mm Circle Centered on the Fovea Using SS-OCTA and SD-OCTA

| N = 40 Eyes	SS-OCTA Mean (SD) [Min, Max]	SD-OCTA Mean (SD) [Min, Max]	Mean Diff (95% CI)	P Value
Square root Total HRF	0.390 (0.170) [0.131−0.835]	0.393 (0.187) [0.146−0.829]	−0.003 (−0.021, 0.015)	0.76

CI = confidence interval; HRF = hyperreflective foci; Max = maximum; Min = minimum; SD = standard deviation; SD-OCTA = spectral-domain OCT angiography; SS-OCTA = swept-source OCT angiography.
Means, standard deviations, minimum and maximum values for the square root total area of the hyperreflective foci on swept-source OCT angiography and spectral-domain OCT angiography scans are presented above. The mean difference (mean diff) of the measurements with its associated 95% confidence interval (cluster bootstrap percentile confidence interval based on 1 000 000 bootstrap samples) was very small and *P* value showed no statistical significance.

manually edited as necessary based on the sub-RPE en face images and B-scan tools available in the algorithm. The 2 graders tried to reach a consensus agreement for the outlines of these lesions in each image and any remaining disagreements were adjudicated by a senior grader (P.J.R.). Only HRF with area measurements of $\geq 1440\ \mu m^2$ were included in the final outlines by the algorithm, which corresponded to lesions measuring ≥ 10 pixels on the SS-OCTA images (1 pixel = 144 μm^2) and 5 pixels on the SD-OCTA images (1 pixel = 294 μm^2). The exact choice of this threshold was established based on the practical limits of a grader's ability to reproducibly grade HRF on both SD- and SS-OCTA scans. The total area of the HRF, also referred as of HRF burden, within the 5-mm circle centered on the fovea was calculated and the measurements from the 2 imaging modalities were compared.

Statistical Analysis

The primary outcome was the square root (sqrt) transformation of the total HRF area (HRF burden). Statistical analyses were performed using R version 4.3.0 (R Foundation for Statistical Computing)[47] with the boot, boot.pval,[48] and tidyverse packages.[49] Agreement between the grading of SS-OCTA and SD-OCTA images using the sqrt of the total HRF area was evaluated with Bland−Altman analysis and Lin's concordance correlation coefficient (r_c), which accounts for the perpendicular deviation of the line of best fit of the paired measurements from the line of equality through the origin. Lin's concordance correlation coefficient also addresses the shortcomings of standard correlation coefficients with respect to the reproducibility-agreement analysis where one measurement can be systematically much higher than the other and
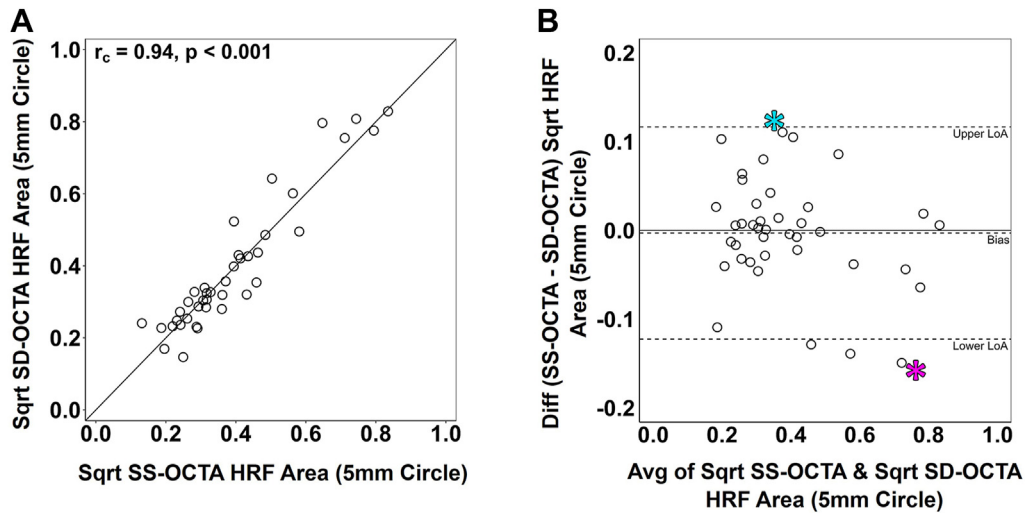
Figure 1. Lin's concordance correlation coefficient (r_c) and Bland−Altman analysis of the sqrt total HRF area measurements in the 5-mm circle centered on the fovea between the SD-OCTA and SS-OCTA scans. **A,** The solid diagonal line represents the line of equality (slope = 1), showing a high concordance between sqrt area measurements of the SS-OCTA and SD-OCTA scans, with a concordance correlation coefficient (r_c) = 0.94 (95% CI: 0.86−0.97; *P* < 0.001). **B,** The Bland−Altman plot shows a small, estimated bias (mean difference) of −0.003 (95% CI: −0.021 to 0.015), with lower LoA: −0.122 (95% CI: −0.154 to −0.084), and upper LoA: 0.117 (95% CI: 0.084−0.142). Cases with larger averaged sqrt total HRF area in the 5-mm circle, especially over 0.50 mm tended to show slightly larger SD-OCTA measurements, which is represented by the case identified with the magenta asterisk (Case #4, Fig. 5). On the opposite side, toward the upper LoA, the blue asterisk (Case #3, Fig. 4) represents the case with the greater difference in favor of larger measurements from SS-OCTA compared with the SD-OCTA scans. However, neither difference was considered statistically or clinically significant. CI = confidence interval; HRF = hyperreflective foci; LoA = limit of agreement; SD-OCTA = spectral-domain OCT angiography; sqrt = square root; SS-OCTA = swept-source OCT angiography.
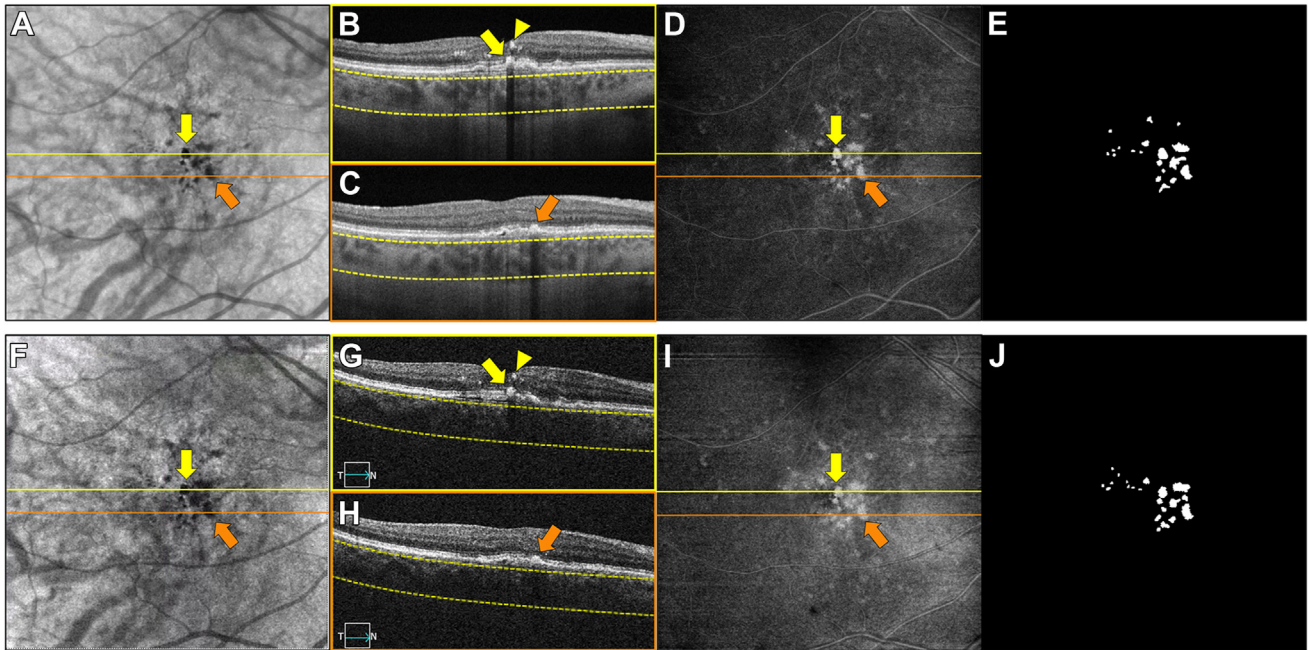
Figure 2. An eye with similar total HRF area measurements within the 5-mm circle centered on the fovea between SS-OCTA and SD-OCTA scans performed on the same day (Case #1). **A** to **E,** show the images obtained using SS-OCTA and **F** to **J,** show the images the images obtained using SD-OCTA. **A, F,** Show the en face structural images that were created for both scan modalities by using a custom sub-RPE slab positioned 64 to 400 μm under BM. **B, C, G, H,** are the B-scan views identified by the colors yellow and orange lines to match the 2 horizontal B-scans shown with the same colors in (**A**) and (**F**). The yellow dashed lines on the B-scans show the segmentation boundaries for the sub-RPE slab. **D, I,** are the en face sum projection images of an OAC slab created from the inner limiting membrane to the BM, and generated by a proprietary, validated semiautomated algorithm that identified and measured the areas of the HRF. **E, J,** Show the final masks created with the above-mentioned algorithm after editing and consensus grading were applied to the OAC sum projection images. **B, G,** B-scans in yellow and (**C, H**) B-scans in orange represent the same anatomic areas respectively from both SS-OCTA and SD-OCTA scans. These B-scans show the HRF along the RPE (see yellow and orange arrows) and the iHRF (see yellow arrowheads) that produce the characteristic hypoTDs in the choroid that correspond on the en face sub-RPE structural image (**A, F**) to the darker areas identified by the yellow and orange arrows. On the en face OAC sum projection image (**D, I**), these foci correspond to the brighter areas identified by the same type of arrows. The hypoTDs caused by the iHRF (yellow arrowheads in **B, G**) overlap with the one caused by the rpeHRF (yellow arrows), hence the total area calculated on the en face image includes both type of HRF lesions. The square root total HRF area from SS-OCTA (**A−E**) was 0.48 mm (total area = 0.23 mm^2) and from SD-OCTA (**F−J**) was 0.49 mm (total area = 0.24 mm^2). BM = Bruch's membrane; HRF = hyperreflective foci; hypoTDs = hypotransmission defects; iHRF = intraretinal hyperreflective foci; OAC = optical attenuation coefficient; RPE = retinal pigment epithelium; rpeHRF = hyperreflective foci along the retinal pigment epithelium; SD-OCTA = spectral-domain OCT angiography; SS-OCTA = swept-source OCT angiography.

yield a high correlation.[50] Cluster bootstrap resampling was used to account for clustering of fellow eyes.[50,51] P values were obtained via confidence interval inversion and a 2-sided P value <0.05 was considered statistically significant.

Results

A total of 40 eyes from 35 patients with nonexudative iAMD were identified for this study. These subjects underwent both SD-OCTA and SS-OCTA imaging on the same day from April 2016 to May 2023. Their ages ranged from 57 to 96 years old (mean age 79.5 with a standard deviation [SD] of 7.8 years) and 57.5% were women.

The mean sqrt of the total HRF area was 0.390 mm (SD: 0.170) on SS-OCTA images and 0.393 mm (SD: 0.187) on SD-OCTA images, with a corresponding mean difference (bias) of −0.003 (95% confidence interval: −0.021 to 0.015; P = 0.76; Table 1). The sqrt total HRF area measurements from both imaging modalities were highly concordant, with an r$_c$ of 0.94 (95% confidence interval:

0.86−0.97; P < 0.001; Figure 1A). The Bland−Altman analysis found a small nonsignificant bias toward SS-OCTA measurements for smaller sqrt total HRF areas and a small nonsignificant bias toward SD-OCTA measurements for larger sqrt total HRF areas (Fig 1B), but, overall, the 2 instruments showed similar measurements. Figures 2 and 3 show 2 examples of eyes with similar sqrt total HRF area between the SS-OCTA and the SD-OCTA scans. In the first case (Figure 2), the sqrt total HRF area on SS-OCTA was 0.48 mm (total area = 0.23 mm^2) and on SD-OCTA was 0.49 mm (total area = 0.24 mm^2). In the second case (Fig 3), the sqrt total HRF area on SS-OCTA was 0.41 mm (total area = 0.17 mm^2) and on SD-OCTA was 0.42 mm (total area = 0.18 mm^2).

In contrast, Figures 4 and 5 show examples of eyes with relatively larger differences between the measured areas on SS-OCTA and SD-OCTA images. The case in Figure 4 corresponds to the one identified by the blue asterisk in the Bland−Altman plot (Fig 1B) and shows the eye with the largest area difference in favor of the SS-OCTA image. In this example, the sqrt total HRF area measured 0.43
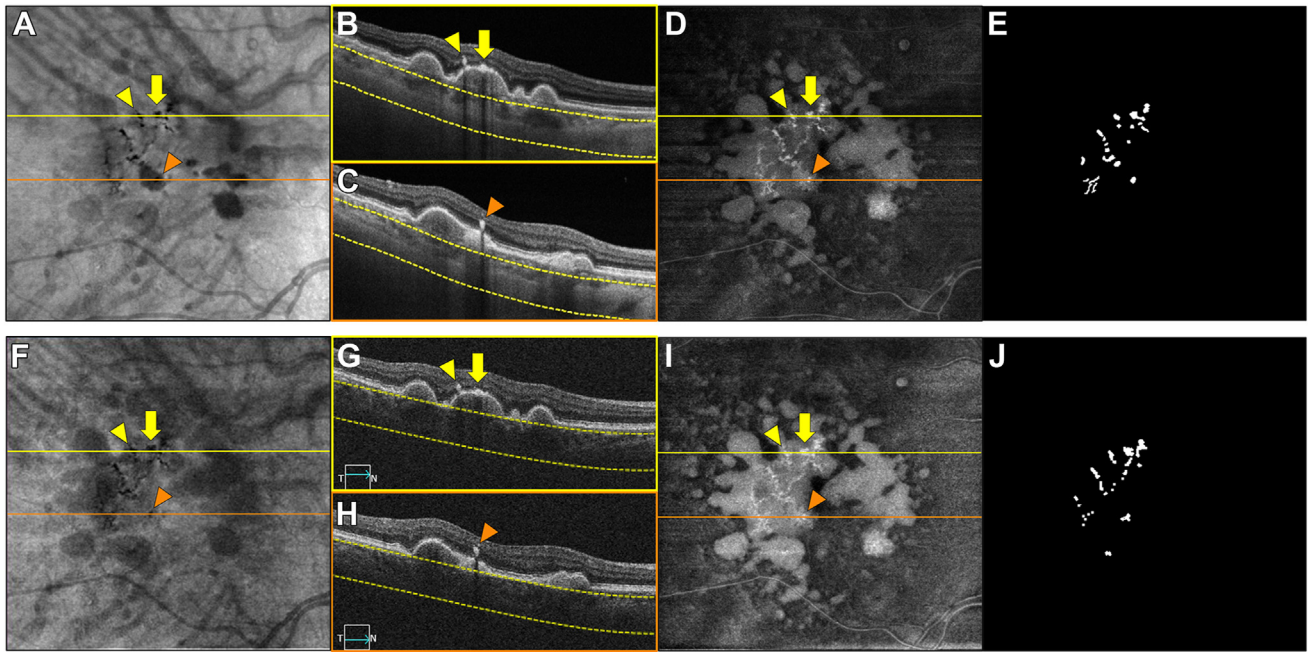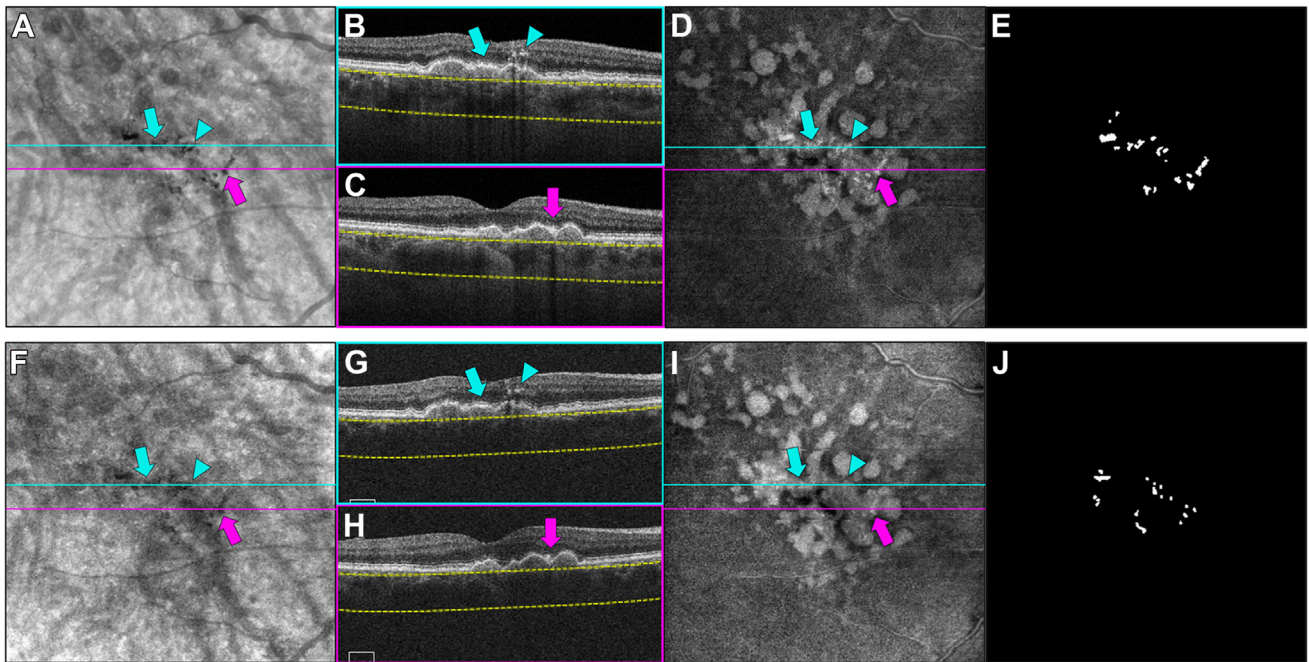
Figure 3. An eye with similar total HRF area measurements in the 5-mm circle centered on the fovea between SS-OCTA and SD-OCTA scans performed on the same day (Case #2). **A** to **E,** show the images obtained using SS-OCTA and **F** to **J,** show the images obtained using SD-OCTA. **A, F,** Show a custom sub-RPE slab positioned 64 to 400 μm under BM. **B, C, G, H,** are the b-scan views identified by the colors yellow and orange to match the two-horizontal b-scan levels with the same colors shown in (**A**) and (**F**). The yellow dashed lines on the B-scans show the segmentation boundaries for the sub-RPE slab. **D, I,** are the en face sum projection images of an OAC slab created from the inner limiting membrane to the BM, and generated by a proprietary, validated semiautomated algorithm that identified and measured the areas of the HRF. **E, J,** Show the final masks created with the above-mentioned algorithm after editing was applied to the OAC sum projection images, after graders' consensus. **B, G,** B-scans in yellow and **C, H,** B-scans in orange, represent the same anatomic areas respectively from both SS-OCTA and SD-OCTA. These show the HRF along the RPE (see yellow arrows), and the intraretinal HRF (yellow and orange arrowheads), which produce a characteristic hypotransmission of light into the choroid that corresponds on the en face sub-RPE structural image (**A, F**) to the darker areas identified by the yellow arrows and arrowheads and the orange arrowheads respectively; and on the en face OAC sum projection (**D, I**) to the corresponding brighter areas identified by the same indicators. The square root total HRF area from SS-OCTA (**A–E**) was 0.41 mm (total area = 0.17 mm^2) and from SD-OCTA (**F–J**) was 0.42 mm (total area = 0.18 mm^2). BM = Bruch's membrane; HRF = hyperreflective foci; OAC = optical attenuation coefficient; RPE = retinal pigment epithelium; SD-OCTA = spectral-domain OCT angiography; SS-OCTA = swept-source OCT angiography.

mm (total area = 0.19 mm^2) on the SS-OCTA image, while on the SD-OCTA image it measured 0.32 mm (total area = 0.10 mm^2). Figure 5 shows the eye with the largest area difference in favor of the SD-OCTA image, which corresponds to the datapoint identified by the magenta asterisk in the Bland−Altman plot (Fig 1B). In this example, the sqrt total HRF area measured on the SS-OCTA image was 0.65 mm (total area = 0.42 mm^2) compared with 0.80 mm (total area = 0.63 mm^2) on the SD-OCTA image.

Discussion

In this study, the total area of the HRF, referred also to as the HRF burden, was measured on sub-RPE slabs from SD-OCTA and SS-OCTA en face images generated from 6 × 6 mm OCTA scans performed on the same patient on the same day and the measurements were compared. The measurements were compared using the sqrt of the area rather than the total area of the HRF to reduce the impact of lesion size on the test-retest SDs and eliminate the dependence of the growth of HRF on the baseline size of the HRF. This is analogous to the use of sqrt root area in

the study of geographic atrophy.[52] The mean difference (bias) in the sqrt total HRF area between the 2 OCTA instruments was very small and was not statistically significant (mean diff = −0.003; P = 0.76; Table 1) with Figure 1A showing a high concordance between the measurements (r_c = 0.94; P < 0.001; Fig 1A). Cases in Figures 2 and 3 illustrate similar measurements. The eye shown in Figure 5 and identified by the magenta asterisk in the Bland−Altman plot (Fig 1B) is a good example of a larger measurement using SD-OCTA imaging. The fact that hypoTDs tend to be larger on the en face SD-OCTA image compared with the SS-OCTA image might be explained by the greater distance between A-scans on the SD-OCTA scan pattern (17 μm) compared with the SS-OCTA scan pattern (12 μm), which could result in an overestimation of the HRF lesions. Also, the lower pixel density in the SD scan pattern could be caused by closely spaced HRF being inadequately resolved and separately quantified. In addition, the choroidal hypotransmission from the hypoTDs may be less well defined compared with the surrounding choroidal reflectivity when using SD-OCTA imaging compared with the better choroidal penetration and less sensitivity roll-off of the SS-OCTA
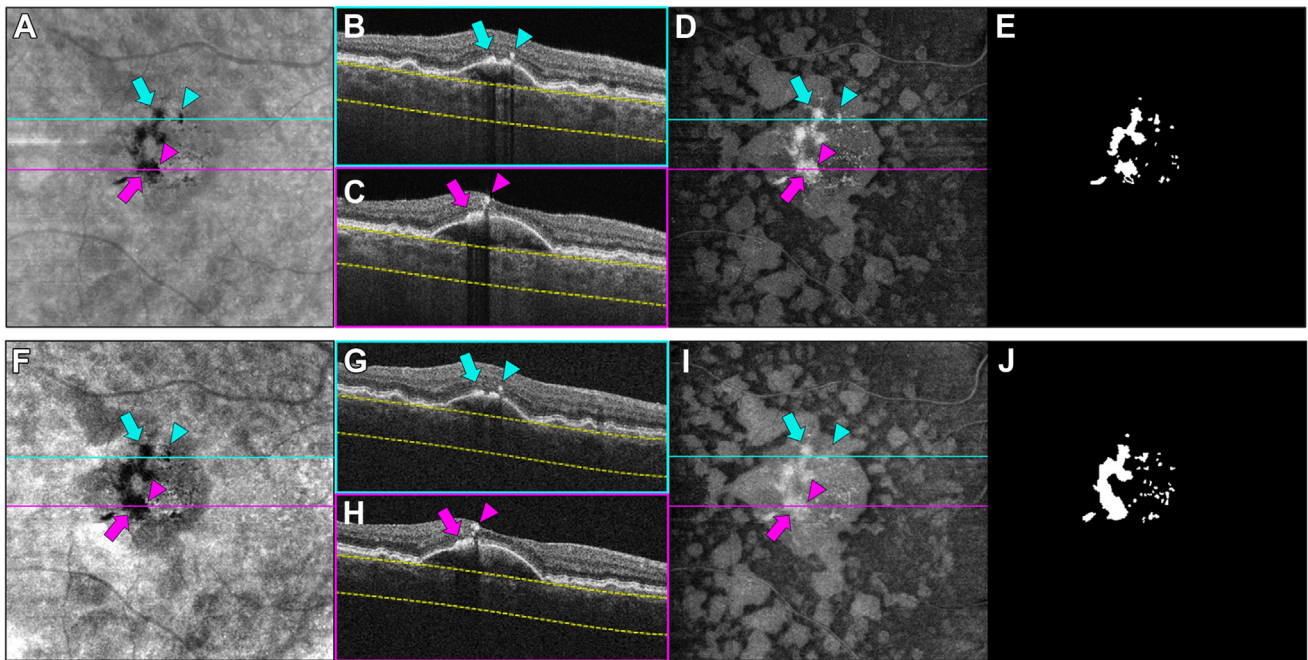
Figure 4. An eye with larger HRF area measurements in the 5-mm circle centered on the fovea with SS-OCTA scans compared with SD-OCTA scans performed on the same subject (Case #3) on the same day. This case corresponds to the one identified by the blue asterisk in the Bland–Altman plot (Fig 1B), representing the case with the greatest difference between the measurements, with HRF area in SS-OCTA larger than in SD-OCTA. **A** to **E**, Show the images obtained using SS-OCTA and **F** to **J**, the images obtained using SD-OCTA. **A, F**, Show a custom sub-RPE slab positioned 64 to 400 μm under BM. **B, C, G, H**, Are the b-scan views identified by the colors blue and magenta to match the 2-horizontal b-scan levels with the same colors shown in (**A**) and (**F**). The yellow dashed lines on the B-scans show the segmentation boundaries for the sub-RPE slab. **D, I**, Are the en face sum projection images of an OAC slab created from the inner limiting membrane to the BM, and generated by a proprietary, validated semiautomated algorithm that identified and measured the areas of the HRF. **E, J**, Show the final masks created with the above-mentioned algorithm after editing was applied to the OAC sum projection images, after graders' consensus. **B, G**, B-scans in blue and **C, H**, B-scans in magenta, represent the same anatomic areas respectively from both SS-OCTA and SD-OCTA. The blue and magenta arrows indicate the HRF along the RPE and the blue arrowheads the intraretinal HRF, which produce a characteristic hypotransmission of light into the choroid that corresponds on the en face sub-RPE structural image (**A, F**) to the darker areas identified by the blue arrows and arrowheads and the magenta arrows respectively; and on the en face OAC sum projection (**D, I**) to the corresponding brighter areas identified by the same indicators. These lesions were easier to detect on the SS-OCTA scans (**A–E**) as compared with the SD-OCTA scans (**F–J**), hence the subsequent differences in the final masks (**E, J**) and quantification of the areas. The square root total HRF area from SS-OCTA (**A–E**) was 0.43 mm (total area = 0.19 mm²) and from SD-OCTA (**F–J**) was 0.32 mm (total area = 0.10 mm²). BM = Bruch's membrane; HRF = hyperreflective foci; OAC = optical attenuation coefficient; RPE = retinal pigment epithelium; SD-OCTA = spectral-domain OCT angiography; SS-OCTA = swept-source OCT angiography.

imaging. This is due to a SS-OCTA center wavelength of 1050 nm compared with the SD-OCTA center wavelength of 840 nm. As a result, SD-OCTA imaging results in more blurred, less well-defined margins and larger area measurements as shown in the B-scans and en face images in Figure 5.

In contrast, the measurements of smaller lesions tended to be slightly larger using SS-OCTA scans than with SD-OCTA scans. The ability to detect smaller HRF on SS-OCTA images can be appreciated in Figure 4 and may also be explained by the denser isotropic spacing between A-scans and B-scans in the SS-OCTA scans, the longer wavelength, and the reduced sensitivity roll-off, which improves the detection of small lesions.[53] As described by Oncel et al,[54] increased inter-B-scan spacing tends to reduce the ability to accurately determine whether iHRF are present in an eye.[54] However, these differences between the measurements from the 2 instruments were neither statistical nor clinically significant.

Overall, both the SS-OCTA and SD-OCTA scans yielded similar results in the measurement of HRF using the same semiautomated algorithm with edited manual outlines. These results encourage the use of a single scan pattern, either SD-OCTA or SS-OCTA scans, for the structural and angiographical imaging of AMD, which provides the convenience of using a single scan pattern to follow AMD progression. Moreover, the OCTA scan pattern offers a denser isotropic scan pattern with a repeated scan at each B-scan position compared with the typical corresponding structural OCT scans, yielding better image quality, and saving the need to acquire separate structural and angiographic scans.[35] Using this strategy to follow eyes with AMD, we had previously found that it was possible to identify the HRF on en face SS-OCTA images,[7] and quantify these lesions using a semiautomated algorithm that incorporated the use of optical attenuation coefficients to accurately estimate their outlines on the en face images.[36] Our present results are consistent with several

Figure 5. An eye with larger HRF area measurements in the 5 mm circle centered on the fovea with SD-OCTA scans compared with SS-OCTA scans performed on the same subject (Case #4) on the same day. This case corresponds to the one identified by the magenta asterisk in the Bland–Altman plot (Fig 1B), representing the case with the largest difference between the measurements, with HRF area in SD-OCTA larger than SS-OCTA. **A** to **E,** Show the images obtained using SS-OCTA and **F** to **J,** the images obtained using SD-OCTA. **A, F,** Show a custom sub-RPE slab positioned 64 to 400 μm under BM. **B, C, G, H,** Are the b-scan views identified by the colors blue and magenta to match the 2-horizontal b-scan levels shown in (**A**) and (**F**) by the blue and magenta lines. The yellow dashed lines on the B-scans show the segmentation boundaries for the sub-RPE slab. **D, I,** Are the en face sum projection images of an OAC slab created from the inner limiting membrane to the BM, and generated by a proprietary, validated semiautomated algorithm that identified and measured the areas of the HRF. **E, J,** show the final masks created with the above-mentioned algorithm after editing has been applied to the OAC sum projection images, after consensus between graders. **B, G,** B-scans in blue and (**C, H**) B-scans in magenta, represent the same anatomic areas respectively from both SS-OCTA and SD-OCTA. The blue and magenta arrows indicate the HRF along the RPE and the blue and magenta arrowheads the intraretinal HRF that has migrated away from the RPE. Both type of HRF, produce a characteristic hypoTD that corresponds on the en face sub-RPE structural image (**A, F**) to the darker areas identified by the blue and magenta arrows and arrowheads respectively; and on the en face OAC sum projection (**D, I**) to the corresponding brighter areas identified by the same indicators. **C, H,** The iHRF (see magenta arrowheads), adjacent to the rpeHRF (see magenta arrows), produce a merged hypoTD in the en face (**A, F**) that seems thicker on the SD-OCTA than the SS-OCTA scans, even when the shadow signal is more obvious in the SS-OCTA B-scans (**C, H**). This is why the final masks (**E, J**) look thicker for the SD-OCTA resulting in a different HRF area measurement between both imaging modalities. The square root total HRF area from SS-OCTA (**A–E**) was 0.65 mm (total area = 0.42 mm^2) and from SD-OCTA (**F–J**) was 0.80 mm (total area = 0.63 mm^2). BM = Bruch's membrane; HRF = hyperreflective foci; hypoTD = hypotransmission of light into the choroid; OAC = optical attenuation coefficient; RPE = retinal pigment epithelium; rpeHRF = hyperreflective foci along the retinal pigment epithelium; SD-OCTA = spectral-domain OCT angiography; SS-OCTA = swept-source OCT angiography.

reports that have shown the feasibility and accuracy of detecting and measuring iHRF using SD-OCT structural scans in lieu of other imaging modalities,[12,21,28,31–33,54–56] although our strategy has the added advantage of measuring the HRF along the RPE and not just in the retina by using the en face OCTA images followed by the confirmatory review of the OCTA B-scans.[7,36] Accounting for both types of HRF is important when assessing risk for disease progression in a more comprehensive way, despite the possible distinctive pathological process that may give rise of these types of HRF. There is current debate on whether the HRF in the retina represent RPE aggregations that have migrated into the neurosensory retina after RPE epithelial mesenchymal transition or if they represent melanosome-laden mononuclear phagocytes.[30,57–59] In any case, even if these type of HRF could have different pathways of development, the common denominator is an underlying sick RPE layer and both are markers of disease progression, especially for the development of macular atrophy.[12,13,18,21,24] Also, both have been directly correlated with the presence of macular hyperPig on multiple imaging modalities as reported by Langinhas et al.[7] An additional benefit of our strategy is that the same scan can be used to detect and quantify other known risk factors that contribute to the development of macular atrophy or exudation such as drusen area and volume,[37,38] calcifying drusen,[39,40] basal laminar deposits,[41] and outer retinal thickness,[42,60] which are best visualized on structural OCT images, as well as features that are best illustrated in the flow OCT images, like perfusion or neovascularization. This approach should increase the efficiency of routine clinical imaging, simplify the design of clinical trials, and reduce the cost of clinical trials designed to study disease progression in nonexudative AMD.[38]

Limitations of this study include a small sample size and the utilization of a semiautomated algorithm that still requires manual editing. However, it is important to note that given very high concordance between the measurements of the sqrt HRF areas using both OCTA modalities, it is unlikely that expanding the sample size would significantly impact our results. It could be argued that the segmentation algorithms employed in this investigation to initialize the manual outlines could possibly introduce a bias in our measurements. However, the graders very carefully reviewed and edited the outlines and any such bias, if present, would be expected to be minimal and not clinically relevant. Given the semiautomatic nature of the algorithm, the need for knowledgeable and trained graders could be a potential limitation of this algorithm in a clinical setting. Another limitation of our grading strategy is the lower limit of detection being set at 10X10 pixels or 1440 μm^2, which corresponded to the smallest region comfortably detected by our graders. While it is possible that future studies might identify smaller lesions as having a higher predictive value for disease progression than those detected by our algorithm, we believe that this is unlikely given the pinpoint appearance of the lesions identified and the typical burden of HRF associated with disease progression. While congruent measurements were obtained using both SD-OCTA and SS-OCTA technologies, for the sake of longitudinal reliability, it is advisable that patients adhere to a single imaging platform when longitudinal imaging is performed, be it SD-OCTA or SS-OCTA. Although this study shows that both SD-OCTA and SS-OCTA scan patterns can be used to measure the macular HRF burden, the current algorithm was only tested on the Zeiss Cirrus SD-OCTA scan pattern, and it is unlikely that the SD-OCTA scan pattern from another spectral domain device will be compatible with the algorithm. While the differences in the quality indices between the paired images could be considered to have had an effect in the HRF measurements, we do not believe any differences had an impact in this regard since the quality indices are determined differently for the 2 instruments, the graders selected only the best quality scans for the analysis, and ultimately, the measurements showed a high degree of concordance.

In summary, both SD-OCTA and SS-OCTA scans can be used to identify and measure HRF in AMD, and we found a strong concordance in the sqrt total area measurements obtained from the 2 instruments. These results suggest that either a single 6 × 6 mm SD-OCTA or a SS-OCTA scan pattern can be used to determine the total macular HRF burden in eyes with AMD.

Footnotes and Disclosures

[1] Department of Ophthalmology, Bascom Palmer Eye Institute, University of Miami Miller School of Medicine, Miami, Florida.

[2] Department of Bioengineering, University of Washington, Seattle, Washington.

[3] Department of Ophthalmology and Visual Science, Yale University School of Medicine, New Haven, Connecticut.

[4] Department of Ophthalmology, IRCCS San Raffaele Scientific Institute, Milan, Italy.

[5] Department of Ophthalmology, Tel Aviv Medical Center, Tel Aviv, Israel.

[6] Department of Ophthalmology, First Affiliated Hospital of Soochow University, Suzhou, Jiangsu, China.

[7] Department of Ophthalmology, University of Washington, Seattle, Washington.

Poster presentation at the 2024 Annual Association for Research in Vision and Ophthalmology Meeting, Seattle, WA. May, 2024.

Disclosure(s):

All authors have completed and submitted the ICMJE disclosures form.

The authors have made the following disclosures:

G.G.: patent − Carl Zeiss Meditec, Inc.

R.K.W.: Grants − Carl Zeiss Meditec, Colgate Palmolive Company, Estee Lauder lnc.; Consultant − Carl Zeiss Meditec, Cyberdontics; Honoraria − Carl Zeiss Meditec; Patents planned, issued or pending − US8, 750, 586, US8, 180, 134, US9, 282, 905, US9, 759, 544, US10, 354, 378, US10, 529, 061.

P.J.R.: Grants − Gyroscope Therapeutics, Stealth BioTherapeutic; Consultant − Annexon, Apellis, Bayer Pharmaceuticals, Boehringer-Ingelheim, Carl Zeiss Meditec, Chengdu Kanghong Biotech, Genentech/Roche, InflammX Therapeutics, Ocudyne, Regeneron Pharmaceuticals, Unity Biotechnology; Shares − Apellis, InflammX, Ocudyne, Valitor.

HUMAN SUBJECTS: Human subjects were included in this study. Patients with age-related macular degeneration were enrolled in ongoing prospective, observational, swept-source OCT (SS-OCT) and spectral-domain OCT (SD-OCT) imaging studies at the Bascom Palmer Eye Institute. The Institutional Review Board of the University of Miami Miller School of Medicine approved the study, and all patients signed an informed consent for both prospective SD-OCT and SS-OCT studies. The study was performed in accordance with the tenets of the Declaration of Helsinki and complied with the Health Insurance Portability and Accountability Act of 1996.

No animal subjects were included in this study.

Author Contributions:

Conception and design: Herrera, Cheng, Attiku, O'Brien, Gregori, Wang, Rosenfeld

Data collection: Herrera, Cheng, Attiku, Hiya, Shen, Liu, Lu, Berni, Trivizki, Li, Gregori, Wang, Rosenfeld

Analysis and interpretation: Herrera, Cheng, Attiku, Hiya, Shen, Liu, Lu, Berni, Trivizki, Li, O'Brien, Gregori, Wang, Rosenfeld

Obtained funding: N/A

Overall responsibility: Herrera, Cheng, Attiku, Hiya, Shen, Liu, Lu, Berni, Trivizki, Li, O'Brien, Gregori, Wang, Rosenfeld

References

1. The age-related eye disease study system for classifying age-related macular degeneration from stereoscopic color fundus photographs: the age-related eye disease study report number 6. *Am J Ophthalmol*. 2001;132:668−681.
2. Ferris FL, Davis MD, Clemons TE, et al. A simplified severity scale for age-related macular degeneration: AREDS Report No. 18. *Arch Ophthalmol*. 2005;123:1570−1574.
3. Cukras C, Agrón E, Klein ML, et al. Natural history of drusenoid pigment epithelial detachment in age-related macular degeneration: age-related eye disease study report No. 28. *Ophthalmology*. 2010;117:489−499.
4. Fleckenstein M, Keenan TDL, Guymer RH, et al. Age-related macular degeneration. *Nat Rev Dis Primers*. 2021;7:31.
5. Ferris 3rd FL, Wilkinson CP, Bird A, et al. Clinical classification of age-related macular degeneration. *Ophthalmology*. 2013;120:844−851.
6. Folgar FA, Chow JH, Farsiu S, et al. Spatial correlation between hyperpigmentary changes on color fundus photography and hyperreflective foci on SDOCT in intermediate AMD. *Invest Ophthalmol Vis Sci*. 2012;53:4626−4633.
7. Laiginhas R, Liu J, Shen M, et al. Multimodal imaging, OCT B-scan localization, and en face OCT detection of macular hyperpigmentation in eyes with intermediate age-related macular degeneration. *Ophthalmol Sci*. 2022;2:100116.
8. Ferrara D, Silver RE, Louzada RN, et al. Optical coherence tomography features preceding the onset of advanced age-related macular degeneration. *Invest Ophthalmol Vis Sci*. 2017;58:3519−3529.
9. Hammer M, Jakob-Girbig J, Schwanengel L, et al. Progressive dysmorphia of retinal pigment epithelium in age-related macular degeneration investigated by fluorescence lifetime imaging. *Invest Ophthalmol Vis Sci*. 2021;62:2.
10. Jaffe GJ, Chakravarthy U, Freund KB, et al. Imaging features associated with progression to geographic atrophy in age-related macular degeneration: classification of atrophy meeting report 5. *Ophthalmol Retina*. 2021;5:855−867.
11. Au A, Santina A, Abraham N, et al. Relationship between drusen height and OCT biomarkers of atrophy in non-neovascular AMD. *Invest Ophthalmol Vis Sci*. 2022;63:24.
12. Christenbury JG, Folgar FA, O'Connell RV, et al. Progression of intermediate age-related macular degeneration with proliferation and inner retinal migration of hyperreflective foci. *Ophthalmology*. 2013;120:1038−1045.
13. Ouyang Y, Heussen FM, Hariri A, et al. Optical coherence tomography−based observation of the natural history of drusenoid lesion in eyes with dry age-related macular degeneration. *Ophthalmology*. 2013;120:2656−2665.
14. Balaratnasingam C, Yannuzzi LA, Curcio CA, et al. Associations between retinal pigment epithelium and drusen volume changes during the lifecycle of large drusenoid pigment epithelial detachments. *Invest Ophthalmol Vis Sci*. 2016;57: 5479−5489.
15. Miura M, Makita S, Sugiyama S, et al. Evaluation of intra-retinal migration of retinal pigment epithelial cells in age-related macular degeneration using polarimetric imaging. *Sci Rep*. 2017;7:3150.
16. Abri AK, Pielen A, Framme C, Junker B. Correlation between hyperreflective foci and clinical outcomes in neovascular age-related macular degeneration after switching to aflibercept. *Invest Ophthalmol Vis Sci*. 2015;56:6448−6455.
17. Nagiel A, Sarraf D, Sadda SR, et al. Type 3 neovascularization: evolution, association with pigment epithelial detachment, and treatment response as revealed by spectral domain optical coherence tomography. *Retina*. 2015;35:638−647.
18. Sleiman K, Veerappan M, Winter KP, et al. Optical coherence tomography predictors of risk for progression to non-neovascular atrophic age-related macular degeneration. *Ophthalmology*. 2017;124:1764−1777.
19. Lei J, Balasubramanian S, Abdelfattah NS, et al. Proposal of a simple optical coherence tomography-based scoring system for progression of age-related macular degeneration. *Graefes Arch Clin Exp Ophthalmol*. 2017;255:1551−1558.
20. Schmidt-Erfurth U, Waldstein SM, Klimscha S, et al. Prediction of individual disease conversion in early AMD using artificial intelligence. *Invest Ophthalmol Vis Sci*. 2018;59: 3199−3208.
21. Nassisi M, Fan W, Shi Y, et al. Quantity of intraretinal hyperreflective foci in patients with intermediate age-related macular degeneration correlates with 1-year progression. *Invest Ophthalmol Vis Sci*. 2018;59:3431−3439.
22. Nassisi M, Lei J, Abdelfattah NS, et al. OCT risk factors for development of late age-related macular degeneration in the fellow eyes of patients enrolled in the HARBOR study. *Ophthalmology*. 2019;126:1667−1674.
23. Waldstein SM, Vogl WD, Bogunovic H, et al. Characterization of drusen and hyperreflective foci as biomarkers for disease progression in age-related macular degeneration using artificial intelligence in optical coherence tomography. *JAMA Ophthalmol*. 2020;138:740−747.
24. Schmidt-Erfurth U, Bogunovic H, Grechenig C, et al. Role of deep learning-quantified hyperreflective foci for the prediction of geographic atrophy progression. *Am J Ophthalmol*. 2020;216:257−270.
25. Fragiotta S, Abdolrahimzadeh S, Dolz-Marco R, et al. Significance of hyperreflective foci as an optical coherence tomography biomarker in retinal diseases: characterization and clinical implications. *J Ophthalmol*. 2021;2021:6096017.
26. Kikushima W, Sakurada Y, Sugiyama A, et al. Characteristics of intermediate age-related macular degeneration with hyper-reflective foci. *Sci Rep*. 2022;12:18420.

27. Nittala MG, Corvi F, Maram J, et al. Risk factors for progression of age-related macular degeneration: population-based amish eye study. *J Clin Med*. 2022;11:5110.

28. Verma A, Corradetti G, He Y, et al. Relationship between the distribution of intra-retinal hyper-reflective foci and the progression of intermediate age-related macular degeneration. *Graefes Arch Clin Exp Ophthalmol*. 2023;261:3437−3447.

29. Ho J, Witkin AJ, Liu J, et al. Documentation of intraretinal retinal pigment epithelium migration via high-speed ultrahigh-resolution optical coherence tomography. *Ophthalmology*. 2011;118:687−693.

30. Balaratnasingam C, Messinger JD, Sloan KR, et al. Histologic and optical coherence tomographic correlates in drusenoid pigment epithelium detachment in age-related macular degeneration. *Ophthalmology*. 2017;124:644−656.

31. Duic C, Pfau K, Keenan TDL, et al. Hyperreflective foci in age-related macular degeneration are associated with disease severity and functional impairment. *Ophthalmol Retina*. 2023;7:307−317.

32. Liu TYA, Wang J, Csaky KG. Correlation between hyper-reflective foci and visual function testing in eyes with intermediate age-related macular degeneration. *Int J Retina Vitreous*. 2023;9:24.

33. Verma A, Nittala MG, Corradetti G, et al. Longitudinal evaluation of the distribution of intraretinal hyper-reflective foci in eyes with intermediate age-related macular degeneration. *Curr Eye Res*. 2024;49:1278−1284.

34. Yehoshua Z, Filho CAAG, Penha FM, et al. Comparison of geographic atrophy measurements from the OCT fundus image and the sub-RPE slab image. *Ophthalmic Surg Lasers Imaging Retina*. 2013;44:127−132.

35. Kashani AH, Chen CL, Gahm JK, et al. Optical coherence tomography angiography: a comprehensive review of current methods and clinical applications. *Prog Retin Eye Res*. 2017;60:66−100.

36. Zhou H, Liu J, Laiginhas R, et al. Depth-resolved visualization and automated quantification of hyperreflective foci on OCT scans using optical attenuation coefficients. *Biomed Opt Express*. 2022;13:4175−4189.

37. Hiya FE, Liu JY, Shen M, et al. Spectral-domain and swept-source OCT angiographic scans yield similar drusen measurements when processed with the same algorithm. *Ophthalmol Sci*. 2023;4:100424.

38. Liu J, Shen M, Laiginhas R, et al. Onset and progression of persistent choroidal hypertransmission defects in intermediate AMD: a novel clinical trial endpoint: hypertransmission defects as a clinical trial endpoint. *Am J Ophthalmol*. 2023;251:11−22.

39. Liu J, Laiginhas R, Shen M, et al. Multimodal imaging and en face OCT detection of calcified drusen in eyes with age-related macular degeneration. *Ophthalmol Sci*. 2022;2:100162.

40. Lu J, Cheng Y, Li J, et al. Automated segmentation and quantification of calcified drusen in 3D swept source OCT imaging. *Biomed Opt Express*. 2023;14:1292−1306.

41. Chu Z, Shi Y, Zhou X, et al. Optical coherence tomography measurements of the retinal pigment epithelium to Bruch membrane thickness around geographic atrophy correlate with growth. *Am J Ophthalmol*. 2022;236:249−260.

42. Zhang Q, Shi Y, Shen M, et al. Does the outer retinal thickness around geographic atrophy represent another clinical biomarker for predicting growth? *Am J Ophthalmol*. 2022;244:79−87.

43. Liu J, Laiginhas R, Corvi F, et al. Diagnosing persistent hypertransmission defects on en face OCT imaging of age-related macular degeneration. *Ophthalmol Retina*. 2022;6:387−397.

44. Laiginhas R, Shi Y, Shen M, et al. Persistent hypertransmission defects detected on en face swept source optical computed tomography images predict the formation of geographic atrophy in age-related macular degeneration. *Am J Ophthalmol*. 2022;237:58−70.

45. Shi Y, Yang J, Feuer W, et al. Persistent hypertransmission defects on en face OCT imaging as a stand-alone precursor for the future formation of geographic atrophy. *Ophthalmol Retina*. 2021;5:1214−1225.

46. Zhou H, Lu J, Chen K, et al. Mitigating the effects of choroidal hyper- and hypo-transmission defects on choroidal vascularity index assessments using optical coherence tomography. *Quant Imaging Med Surg*. 2022;12:2932−2946.

47. R: a language and environment for statistical computing. Version Version 4.4.0. R Foundation for Statistical Computing. https://www.R-project.org/; 2023. Accessed June 30, 2023.

48. Bootstrap p-Values. Version 0.5. CRAN. https://cran.r-project.org/web/packages/boot.pval/boot.pval.pdf; 2023. Accessed June 30, 2023.

49. Hadley WMA, Bryan J, Chang W, et al. Welcome to the tidyverse. *J Open Source Softw*. 2019;4:1686.

50. Lin LI. A concordance correlation coefficient to evaluate reproducibility. *Biometrics*. 1989;45:255−268.

51. Bland JM, Altman DG. Statistical methods for assessing agreement between two methods of clinical measurement. *Lancet*. 1986;1:307−310.

52. Yehoshua Z, Rosenfeld PJ, Gregori G, et al. Progression of geographic atrophy in age-related macular degeneration imaged with spectral domain optical coherence tomography. *Ophthalmology*. 2011;118:679−686.

53. Miller AR, Roisman L, Zhang Q, et al. Comparison between spectral-domain and swept-source optical coherence tomography angiographic imaging of choroidal neovascularization. *Invest Ophthalmol Vis Sci*. 2017;58:1499−1505.

54. Oncel D, Manafi N, Nittala MG, et al. Effect of OCT B-scan density on sensitivity for detection of intraretinal hyper-reflective foci in eyes with age-related macular degeneration. *Curr Eye Res*. 2022;47:1294−1299.

55. Kang D, Lee YJ, Nam KT, et al. Hyperreflective foci distribution in eyes with dry age-related macular degeneration with subretinal drusenoid deposits. *Graefes Arch Clin Exp Ophthalmol*. 2023;261:2821−2828.

56. Sassmannshausen M, Vaisband M, von der Emde L, et al. Hyper-Reflective foci in intermediate age-related macular degeneration: spatial abundance and impact on retinal morphology. *Invest Ophthalmol Vis Sci*. 2023;64:20.

57. Zhou M, Geathers JS, Grillo SL, et al. Role of epithelial-mesenchymal transition in retinal pigment epithelium dysfunction. Review. *Front Cell Dev Biol*. 2020;8:501.

58. Cao D, Leong B, Messinger JD, et al. Hyperreflective foci, optical coherence tomography progression indicators in age-related macular degeneration, include transdifferentiated retinal pigment epithelium. *Invest Ophthalmol Vis Sci*. 2021;62:34.

59. Augustin S, Lam M, Lavalette S, et al. Melanophages give rise to hyperreflective foci in AMD, a disease-progression marker. *J Neuroinflammation*. 2023;20:28.

60. Lu J, Cheng Y, Hiya FE, et al. Deep-learning-based automated measurement of outer retinal layer thickness for use in the assessment of age-related macular degeneration, applicable to both swept-source and spectral-domain OCT imaging. *Biomed Opt Express*. 2024;15:413−427.

Comparison between Spectral-domain and Swept-source OCT Angiography Scans for the Measurement of Hyperreflective Foci in Age-related Macular Degeneration

Gissel Herrera, MD, Yuxuan Cheng, PhD, Yamini Attiku, MD, Farhan E. Hiya, MD, Mengxi Shen, MD, PhD, Jeremy Liu, MD, Jie Lu, PhD, Alessandro Berni, MD, Omer Trivizki, MD, Jianqing Li, MD, Robert C. O'Brien, PhD, Giovanni Gregori, PhD, Ruikang K. Wang, PhD, Philip J. Rosenfeld, MD, PhD

Spectral-domain and swept-source OCT angiography scans were processed using the same semiautomated algorithm and provided similar results for the measurement of hyperreflective foci in eyes with dry age-related macular degeneration.